J. Fluid Mech. (2008), *vol.* 603, *pp.* 391–411.
doi:10.1017/S0022112008001122 Printed in the United Kingdom

On the rotational compressible Taylor flow in injection-driven porous chambers

BRIAN A. MAICKE AND JOSEPH MAJDALANI†

Department of Mechanical, Aerospace, and Biomedical Engineering, University of Tennessee Space Institute, Tullahoma, TN 37388, USA

(Received 31 January 2006 and in revised form 15 February 2008)

This work considers the compressible flow field established in a rectangular porous channel. Our treatment is based on a Rayleigh–Janzen perturbation applied to the inviscid steady two-dimensional isentropic flow equations. Closed-form expressions are then derived for the main properties of interest. Our analytical results are verified via numerical simulation, with laminar and turbulent models, and with available experimental data. They are also compared to existing one-dimensional theory and to a previous numerical pseudo-one-dimensional approach. Our analysis captures the steepening of the velocity profiles that has been reported in several studies using either computational or experimental approaches. Finally, explicit criteria are presented to quantify the effects of compressibility in two-dimensional injection-driven chambers such as those used to model slab rocket motors.

1. Introduction

Berman (1953) first treated the incompressible flow through a permeable channel by perturbing a similarity solution for small wall injection or suction. Taylor (1956) extended the idea by using an integral method to describe the flow through not only rectangular channels, but also through tubes, cones and wedges. Yuan (1956) considered Berman's original work and sought an asymptotic expansion valid for large injection Reynolds numbers. Proudman (1960) extended the large-Reynolds-number solution by considering arbitrary strength injection or suction for either wall of a rectangular chamber.

The study of the permeable walled channel has since been used to investigate a wide array of practical problems. Taylor's groundbreaking work was inspired by the drying of paper in an automated paper mill. Berman was motivated by the need for modelling isotope separation. Yuan (1959) and Peng & Yuan (1965) have studied the flow as a means of controlling temperature via sweat cooling. Our study shares the same objectives that led Culick (1966), Traineau, Hervat & Kuentamann (1986), and Balakrishnan, Liñán & Williams (1992) to devise non-reactive formulations for the internal flow field of a solid rocket motor.

Taylor's analysis of the permeable walled channel furnished a reliable approximation to the core flow inside a solid rocket motor. This was later used at the foundation of many studies seeking to determine (*a*) the ensuing unsteady wave motion or (*b*) the flow instability (e.g. Beddini & Roberts 1988, 1992; Staab & Kassoy 1996; Casalis,

†Author to whom correspondence should be addressed: maji@utsi.edu.

Avalon & Pineau 1998). While Taylor's solution was inviscid, the normal injection condition secured at the sidewall enabled the fluid motion to retain some of the features we normally reserve for a viscous flow. To date, Taylor's incompressible model remains one of the most cited and used in solid rockets. It has been considered by Traineau *et al.* (1986), Balakrishnan *et al.* (1991), Beddini & Roberts (1992), Apte & Yang (2001), Balachandar, Buckmaster & Short (2001), Zhou & Majdalani (2002), Najjar *et al.* (2003) and many others. Two key factors justify its ubiquitous use: the suitability of non-reactive models to simulate the idealized environment in a rocket motor and the validity of using a non-deformable permeable chamber with non-regressing walls. The first factor may be attributed to propellant heat release being confined to a relatively thin flame zone forming above the burning surface (see Chu, Yang & Majdalani 2003). The second factor may be associated with the weak sensitivity of the streamline curvature to the wall regression rate. As shown by Majdalani, Vyas & Flandro (2002), the effect of propellant regression is small in the operational range of most motors.

The motivation for extending the solution to include compressibility is clear. While previous studies have attempted to determine the effects of compressibility in solid rocket motors, none of these have managed to capture the fully two-dimensional behaviour in closed form. The most notable of these are analyses by Flandro (1980), Traineau *et al.* (1986), King (1987), Balakrishnan *et al.* (1992) and Gany & Aharon (1999). Most are pseudo-one-dimensional or limited to numerical integral formulations; moreover, studies with analytical solutions often bear more severe limitations than those imposed in the present work. Clearly, the quest for a compressible analogue to the Taylor profile would be valuable in advancing the theory of internal rotational compressible flow where most problems are solved numerically. Furthermore, with increases in computational power and complexity in available solvers, more accurate and extensive analytical models are becoming desirable to verify the efficacy of new computational routines. Along similar lines, a compressible steady flow model can help investigators to recast the time-dependent flow formulation in rocket motors; the existing relations represent waves that are strongly affected by compressibility (see Majdalani 2001). Finally, a compressible Taylor representation could be applied to the nozzleless motor concept. As described by Gany & Aharon (1999), the nozzleless motor gains in simplicity what it lacks in power.

Traineau *et al.* (1986) tackled this problem numerically using a two-dimensional integration of the Euler equations via a finite volume predictor–corrector method; they also provided useful experimental results. Vuillot & Avalon (1991) solved the two-dimensional laminar compressible unsteady Navier–Stokes equations to understand the effects of compressibility on the acoustic boundary layers in solid rocket motors. Wasistho, Balachandar & Moser (2004) conducted full numerical simulations in an attempt to quantify the effects of compressibility on the transition to turbulent flow.

The first analytical method used in this context is the Prandtl–Glauert expansion (see Shapiro 1953). The velocities of interest are expanded in a series of a shape parameter. These perturbed equations are then solved via traditional methods to determine the solution to the flow field. Kaplan (1943, 1944, 1946) has successfully applied the Prandtl–Glauert expansion to a number of different external flows.

In work more applicable to this study, a variant of the Prandtl–Glauert technique is used by Balakrishnan *et al.* (1992) in a slender rocket motor. They expand the governing equations in terms of the shape parameter, h/a, where h is the height of the motor and a is the length. For slender motors, this term is small, thus reducing the truncation error in Balakrishnan's pseudo-two-dimensional approach. Following an

Abel inversion (see also Traineau *et al.* 1986), a single equation is obtained that can be readily integrated to determine the pressure distribution with respect to X, where X is a strained coordinate. This approach provides a benchmark for compressible rocket studies. By reducing the problem to the numerical evaluation of a simple integral, the technique in question proves to be much less computationally intensive than that employed by Wasistho *et al.* (2004). The latter rely on the numerical integration of multidimensional Navier–Stokes equations to obtain a compressible flow representation that conforms to the results predicted by Balakrishnan *et al.* (1992).

Our method of choice is the Rayleigh–Janzen perturbation expansion. So named after the work presented by Janzen (1913) and Rayleigh (1916) in solving compressible flows, this technique requires all dependent variables to be expanded in a series of the Mach number squared. The expanded variables are then substituted into the modelled equations and segregated in order of the Mach number. The linearized equations are then solved by traditional methods to determine the explicit solution to the problem. Unlike the Prandtl–Glauert expansion, this method is not restricted by the size of the motor, making it ideal for handling a wide range of aspect ratios. Furthermore, its requirement for a small characteristic wall Mach number is assured in the range of rocket motor operation. The Rayleigh–Janzen method can thus render solutions that are valid over the entire range of motor aspect ratios and operating conditions.

A form of the Rayleigh–Janzen technique was used by Flandro (1980) in the context of a compressible internal-burning solid rocket motor. However, Flandro solves quasi-one-dimensional forms of the governing equations; his solution is limited by its inability to satisfy the compressible first-order vorticity transport equation. The Rayleigh–Janzen expansion has been applied successfully by Majdalani (2005, 2007) to determine the compressible analogue to the Taylor–Culick flow field in cylindrical geometry and by Maicke & Majdalani (2006) in a rectangular context. While the Rayleigh–Janzen method has been used to analyse other flow fields, notably the work on Hill's spherical vortex by Moore & Pullin (1998) and the Stuart vortex by Meiron, Moore & Pullin (2000), it has not been widely applied to internal flow problems; this leaves open the possibility of using this approach in other previously untreated cases, such as the star-fin or wagon-wheel grain configurations.

What follows is our plan for the compressible injection-driven channel-flow analysis. In §2, the geometric model is defined and the limiting assumptions are introduced. Section 3 delineates the Rayleigh–Janzen expansion and illustrates the solution methodology. The results of the study are presented in §4, complete with comparisons to previous models and both numerical and experimental verifications. Design criteria and performance characteristics are also derived. Section 5 brings the study to its conclusion, summarizing the results and discussing possible extensions and outlook towards future work.

2. Problem definition

2.1. *Geometry*

To model the slab rocket, a rectangular chamber of length L_0 and half-height of h is used (figure 1). The origin of the coordinate system describing the domain is located at the centre of the headwall. The spatial variables $\bar{x}$ and $\bar{y}$ are defined as the directions parallel and normal to the centre-axis. Taking advantage of symmetry, a solution can be obtained for the top half of the chamber, namely $0 \leqslant \bar{y} \leqslant h$ and $0 \leqslant \bar{x} \leqslant L_0$, and mirrored across the centre-axis.

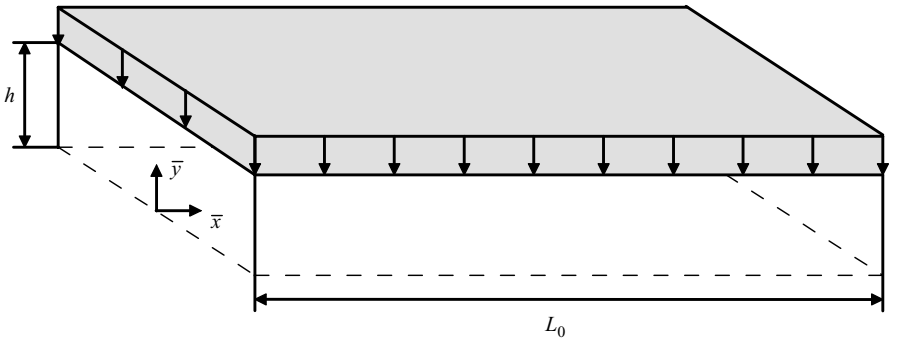

FIGURE 1. Porous channel with an inert headwall.

Along the sidewalls, a uniform injection velocity of U_w is imposed. While there are any number of factors that could affect the local velocity at the propellant surface, density fluctuations, localized non-homogeneity of the propellant, and erosive burning to name a few, this constraint gives a reasonable approximation of the injection mechanism at the propellant surface. The headwall of the motor is solid and inert, allowing for zero normal velocity at the headwall. The resulting model corresponds to the steady inviscid compressible and non-heat-conducting flow of an ideal gas.

2.2. *Non-dimensional formulation*

To facilitate the analysis, it is prudent to non-dimensionalize the variables of interest. A standard methodology is employed resulting in the following parameters:

$$\begin{gathered} x = \frac{\bar{x}}{h}, \quad y = \frac{\bar{y}}{h}, \quad u = \frac{\bar{u}}{U_w}, \quad v = \frac{\bar{v}}{U_w}, \quad p = \frac{\bar{p}}{p_0}, \\ T = \frac{\bar{T}}{T_0}, \quad \rho = \frac{\bar{\rho}}{\rho_0}, \quad \psi = \frac{\bar{\psi}}{U_w \rho_0 h}, \quad \boldsymbol{\Omega} = \frac{\bar{\boldsymbol{\Omega}} h}{U_w}, \quad \nabla = h\bar{\nabla}, \end{gathered} \tag{2.1}$$

where the bold symbol denotes a vector quantity, the overbar indicates a dimensional variable, and the subscript '0' describes a reference condition at the headwall. Given this normalization, the compressible streamfunction and velocities become

$$u = \frac{1}{\rho}\frac{\partial \psi}{\partial y}, \qquad v = -\frac{1}{\rho}\frac{\partial \psi}{\partial x}. \tag{2.2}$$

These relations are substituted into the vorticity definition to provide

$$\frac{\partial^2 \psi}{\partial x^2} + \frac{\partial^2 \psi}{\partial y^2} = \frac{1}{\rho}(\nabla \rho \cdot \nabla \psi) - \Omega \rho. \tag{2.3}$$

In order to solve (2.3), another expression relating vorticity to the streamfunction is required for the right-hand side of the equation to be fully determined. To that end, we may apply the vorticity transport equation via

$$\nabla \times (\boldsymbol{U} \times \boldsymbol{\Omega}) = \frac{1}{\gamma M_w^2 \rho^2} \nabla \rho \times \nabla p, \tag{2.4}$$

where the velocity vector is denoted as $\boldsymbol{U} = u\hat{i} + v\hat{j}$. The momentum equation may then be solved to determine the pressure from

$$\rho\nabla\left[\frac{1}{2\rho^2}(\nabla\psi\cdot\nabla\psi)\right] + \Omega\nabla\psi = -\frac{\nabla p}{\gamma M_w^2}. \tag{2.5}$$

Finally, to bring closure to the problem, we may use

$$\rho = p^{1/\gamma}, \quad T = p^{(\gamma-1)/\gamma}. \tag{2.6}$$

Equation (2.6) is, of course, contingent on the flow being isentropic and calorically perfect.

Our boundary conditions stem from the physical determination of the system. Since the injection of the propellant at the sidewalls is normal to the surface, there is no axial flow at the wall. The headwall of the chamber is inert, providing the second condition. A uniform injection velocity is imposed at the sidewalls. Symmetry provides the last boundary condition. Mathematically, these boundary conditions translate into

$$\bar{u}(\bar{x}, h) = 0, \quad \bar{u}(0, \bar{y}) = 0, \quad \bar{v}(\bar{x}, h) = -U_w, \quad \bar{v}(\bar{x}, 0) = 0, \tag{2.7}$$

or, equivalently,

$$u(x, 1) = 0, \quad u(0, y) = 0, \quad v(x, 1) = -1, \quad v(x, 0) = 0. \tag{2.8}$$

2.3. *Perturbation expansion*

In order to solve (2.3)–(2.6), a Rayleigh–Janzen perturbation may be applied. This requires expanding:

$$\left.\begin{array}{ll} u(x, y) = u_0 + M_w^2 u_1 + O(M_w^4), & \rho(x, y) = 1 + M_w^2\rho_1 + M_w^4\rho_2 + O(M_w^6), \\ v(x, y) = v_0 + M_w^2 v_1 + O(M_w^4), & p(x, y) = 1 + M_w^2 p_1 + M_w^4 p_2 + O(M_w^6), \\ \psi(x, y) = \psi_0 + M_w^2\psi_1 + O(M_w^4), & T(x, y) = 1 + M_w^2 T_1 + M_w^4 T_2 + O(M_w^6), \\ \multicolumn{2}{c}{\boldsymbol{\Omega}(x, y) = \boldsymbol{\Omega}_0 + M_w^2\boldsymbol{\Omega}_1 + O(M_w^4).} \end{array}\right\} \tag{2.9}$$

The perturbation expansions from (2.9) may be substituted into (2.2)–(2.6), and then sorted by order of magnitude. Substitution into (2.2) produces

$$O(1) : u_0 = \frac{\partial\psi_0}{\partial y}, \quad O(M_w^2) : u_1 = \frac{\partial\psi_1}{\partial y} - \rho_1\frac{\partial\psi_0}{\partial y}. \tag{2.10}$$

The same approach may be applied to the crossflow velocity v to yield

$$O(1) : v_0 = -\frac{\partial\psi_0}{\partial x}, \quad O(M_w^2) : v_1 = \rho_1\frac{\partial\psi_0}{\partial x} - \frac{\partial\psi_1}{\partial x}. \tag{2.11}$$

By substituting (2.1) into (2.3)–(2.6) and segregating the leading-order terms, we obtain

$$O(1) : \frac{\partial^2\psi_0}{\partial y^2} + \frac{\partial^2\psi_0}{\partial x^2} = -\Omega_0, \tag{2.12a}$$

$$O(M_w^2) : \nabla\times(\boldsymbol{U}_0\times\boldsymbol{\Omega}_0) = 0, \tag{2.12b}$$

$$O(M_w^2) : -\frac{\nabla p_1}{\gamma} = \nabla\left(\frac{\nabla\psi_0\cdot\nabla\psi_0}{2}\right) + \Omega_0\nabla\psi_0, \tag{2.12c}$$

$$O(M_w^2) : \rho_1 = \frac{p_1}{\gamma}, \tag{2.12d}$$

$$O(M_w^2) : T_1 = \frac{\gamma - 1}{\gamma} p_1. \tag{2.12e}$$

Similarly, the leading-order expansion of the boundary conditions, when expressed in terms of the streamfunction, becomes

$$\frac{\partial \psi_0(x,1)}{\partial y} = 0, \quad \frac{\partial \psi_0(0,y)}{\partial y} = 0, \quad \frac{\partial \psi_0(x,1)}{\partial x} = -1, \quad \frac{\partial \psi_0(x,0)}{\partial x} = 0. \tag{2.13}$$

The first-order governing equations may be obtained by collecting $O(M_w^2)$ and $O(M_w^4)$ terms of the expanded (2.3)–(2.6); we extract

$$O(M_w^2) : \frac{\partial^2 \psi_1}{\partial y^2} + \frac{\partial^2 \psi_1}{\partial x^2} = \nabla \rho_1 \cdot \nabla \psi_0 - \Omega_0 \rho_1 - \Omega_1, \tag{2.14a}$$

$$O(M_w^4) : \nabla \times (\boldsymbol{U}_0 \times \boldsymbol{\Omega}_1) + \nabla \times (\boldsymbol{U}_1 \times \boldsymbol{\Omega}_0) = \nabla \rho_1 \times \nabla p_1, \tag{2.14b}$$

$$O(M_w^4) : -\frac{\nabla p_2}{\gamma} = \nabla \left[(\nabla \psi_0 \cdot \nabla \psi_1) - \rho_1 (\nabla \psi_0 \cdot \nabla \psi_0) \right] + \rho_1 \nabla \left(\frac{\nabla \psi_0 \cdot \nabla \psi_0}{2} \right) + \Omega_0 \nabla \psi_1 + \Omega_1 \nabla \psi_0, \tag{2.14c}$$

$$O(M_w^4) : \rho_2 = \frac{p_2}{\gamma} + \frac{1 - \gamma}{\gamma} p_1^2, \tag{2.14d}$$

$$O(M_w^4) : T_2 = \frac{\gamma - 1}{\gamma} p_2 + \frac{1 - \gamma}{2\gamma^2} p_1^2. \tag{2.14e}$$

Since the boundary conditions must be satisfied by the leading-order equation, a set of homogeneous boundary conditions must be imposed from this point forward, specifically,

$$\left.\begin{aligned} \rho_1 \frac{\partial \psi_0(x,1)}{\partial x} - \frac{\partial \psi_1(x,1)}{\partial x} = 0, \quad \frac{\partial \psi_1(x,1)}{\partial y} - \rho_1 \frac{\partial \psi_0(x,1)}{\partial y} = 0, \\ \rho_1 \frac{\partial \psi_0(x,0)}{\partial x} - \frac{\partial \psi_1(x,0)}{\partial x} = 0, \quad \frac{\partial \psi_1(0,y)}{\partial y} - \rho_1 \frac{\partial \psi_0(0,y)}{\partial y} = 0. \end{aligned}\right\} \tag{2.15}$$

3. Solution

3.1. *Leading-order solution*

In order to solve (2.12*a*), we must determine an additional relationship between the vorticity and the streamfunction using the vorticity transport equation. Expanding (2.12*b*) and substituting the streamfunction in place of velocity, we find

$$\frac{\partial \psi_0}{\partial y} \frac{\partial \Omega_0}{\partial x} = \frac{\partial \psi_0}{\partial x} \frac{\partial \Omega_0}{\partial y}. \tag{3.1}$$

Equation (3.1) will be satisfied when

$$\Omega_0 = C^2 \psi_0. \tag{3.2}$$

With (3.2) providing the link between vorticity and the streamfunction, it is now possible to solve (2.12*a*). The streamfunction may then be used to determine the leading-order quantities of all parameters of interest, thus recovering Taylor's

incompressible solution to the slab rocket motor. With this in mind, (3.2) may be substituted into (2.12*a*) such that

$$\frac{\partial^2\psi_0}{\partial y^2} + \frac{\partial^2\psi_0}{\partial x^2} + C^2\psi_0 = 0. \tag{3.3}$$

Applying separation of variables yields the leading-order term

$$\psi_0 = x\sin\left(\tfrac{1}{2}\pi y\right). \tag{3.4}$$

The determination of the first-order pressure follows directly once the leading-order streamfunction is known. Removing the vorticity term from the equation by substituting (3.2), the result is an equation that may be integrated directly for the pressure. After some trigonometric simplifications, we find

$$p_1 = -\tfrac{1}{2}\gamma\left[\tfrac{1}{4}\pi^2x^2 + \sin^2\left(\tfrac{1}{2}\pi y\right)\right]. \tag{3.5}$$

Determining the first-order density and temperature requires the substitution of (3.5) into (2.12*d*) and (2.12*e*), respectively. We get

$$\rho_1 = -\tfrac{1}{2}\left[\tfrac{1}{4}\pi^2x^2 + \sin^2\left(\tfrac{1}{2}\pi y\right)\right],\ T_1 = \tfrac{1}{2}(1-\gamma)\left[\tfrac{1}{4}\pi^2x^2 + \sin^2\left(\tfrac{1}{2}\pi y\right)\right]. \tag{3.6}$$

3.2. *First-order solution*

The first-order correction follows the same general outline as the leading-order analysis; we solve the vorticity transport equation, followed by the vorticity equation, the momentum equation for the pressure, and then finally the density and temperature from the isentropic relations. However, the first-order equations are distinctly more elaborate. It is not until the first-order corrections are determined that we can capture the effects of compressibility on the internal flow field.

3.2.1. *First-order vorticity transport*

The vorticity transport equation is used to determine a relationship between vorticity and the streamfunction at the first order. To that end, (2.14*b*) is examined. Since p_1 and ρ_1 differ only by a constant, γ, the right-hand side of (2.14*b*) vanishes given that the cross-product between two collinear vectors is null. We are left with

$$\nabla\times(\boldsymbol{U}_0\times\boldsymbol{\Omega}_1) + \nabla\times(\boldsymbol{U}_1\times\boldsymbol{\Omega}_0) = 0. \tag{3.7}$$

Vector operations may then be expanded into

$$\frac{\partial}{\partial x}(u_0\Omega_1 + u_1\Omega_0) + \frac{\partial}{\partial y}(v_0\Omega_1 + v_1\Omega_0) = 0. \tag{3.8}$$

To identify the desired relationship between the first-order vorticity and streamfunction, (2.10), (2.11) and (3.2) are substituted. We obtain

$$\begin{aligned}&\frac{\partial}{\partial x}\left[\frac{\partial\psi_0}{\partial y}\Omega_1 + \frac{\pi^2}{4}\left(\frac{\partial\psi_1}{\partial y} - \rho_1\frac{\partial\psi_0}{\partial y}\right)\psi_0\right]\\ &\quad+\frac{\partial}{\partial y}\left[-\frac{\partial\psi_0}{\partial x}\Omega_1 + \frac{\pi^2}{4}\left(\rho_1\frac{\partial\psi_0}{\partial x} - \frac{\partial\psi_1}{\partial x}\right)\psi_0\right] = 0.\end{aligned} \tag{3.9}$$

The derivatives are then evaluated and the expanded equation is simplified to yield

$$\frac{\partial\Omega_1}{\partial x}\frac{\partial\psi_0}{\partial y} - \frac{\partial\Omega_1}{\partial y}\frac{\partial\psi_0}{\partial x} = \tfrac{1}{4}\pi^2\left[\psi_0\left(\frac{\partial\rho_1}{\partial x}\frac{\partial\psi_0}{\partial y} - \frac{\partial\rho_1}{\partial y}\frac{\partial\psi_0}{\partial x}\right) + \frac{\partial\psi_1}{\partial x}\frac{\partial\psi_0}{\partial y} - \frac{\partial\psi_1}{\partial y}\frac{\partial\psi_0}{\partial x}\right]. \tag{3.10}$$

The method of determining a relation without fully solving the equation is not as practical for such a complex equation. However, further simplifications become possible after realizing that the first-order vorticity is an extension of the leading-order term. It is not enough to set $\Omega_1 = \pi^2\psi_1/4$ as this expression does not satisfy (3.10). To find the proper expansion we must let

$$\Omega_1 = \tfrac{1}{4}\pi^2\psi_1 + \Omega_c, \tag{3.11}$$

where Ω_c is an additional correction. Equation (3.11) is then substituted into (3.10) to provide

$$\frac{\partial\Omega_c}{\partial x}\frac{\partial\psi_0}{\partial y} - \frac{\partial\Omega_c}{\partial y}\frac{\partial\psi_0}{\partial x} = \tfrac{1}{4}\pi^2\psi_0\left(\frac{\partial\rho_1}{\partial x}\frac{\partial\psi_0}{\partial y} - \frac{\partial\rho_1}{\partial y}\frac{\partial\psi_0}{\partial x}\right), \tag{3.12}$$

whence

$$\Omega_c = \pm\tfrac{1}{32}\pi^2 x\left[\pi^2x^2\sin\left(\tfrac{1}{2}\pi y\right) + 4\sin^2\left(\tfrac{1}{2}\pi y\right)\right] + f(\psi_0) \tag{3.13}$$

and f is some function that will be determined later to ensure that the first-order equation satisfies all of the requisite conditions.

3.2.2. *First-order vorticity*

With the addition of (3.13), it is now possible to revisit (2.14*a*) as the vorticity equation is now expressible in terms of the first-order streamfunction. Substitution of (3.2), (3.4), (3.6) and (3.13) into (2.14*a*) gives

$$\frac{\partial^2\psi_1}{\partial y^2} + \frac{\partial^2\psi_1}{\partial x^2} + \tfrac{1}{4}\pi^2\psi_1 = -\tfrac{1}{4}\pi^2 x\sin\left(\tfrac{1}{2}\pi y\right)\left[-\tfrac{1}{4}\pi^2x^2 + 1 + \cos(\pi y)\right] - f(\psi_0). \tag{3.14}$$

It is possible to solve (3.14) by assuming an ansatz and then solving two coupled ordinary differential equations, rather than the single partial differential equation. After the work shown in the Appendix, we retrieve

$$\psi_1 = -\tfrac{1}{48}x\sin\left(\tfrac{1}{2}\pi y\right)\left\{\pi^2x^2\left[3 + \cos(\pi y)\right] + 3\left[7 - \cos(\pi y)\right]\right\}. \tag{3.15}$$

3.2.3. *Second-order thermodynamic variables*

In order to determine the second-order pressure term, it is advantageous to expand the vector equation presented in (2.14*c*) into two scalar equations:

$$\begin{aligned}\frac{\partial p_2}{\partial x} = {} & -\gamma\frac{\partial}{\partial x}\left\{\frac{\partial\psi_0}{\partial x}\frac{\partial\psi_1}{\partial x} + \frac{\partial\psi_0}{\partial y}\frac{\partial\psi_1}{\partial y} - \rho_1\left[\left(\frac{\partial\psi_0}{\partial x}\right)^2 + \left(\frac{\partial\psi_0}{\partial y}\right)^2\right]\right\} \\ & + \gamma\left\{\tfrac{1}{2}\rho_1\frac{\partial}{\partial x}\left[\left(\frac{\partial\psi_0}{\partial x}\right)^2 + \left(\frac{\partial\psi_0}{\partial y}\right)^2\right] + \Omega_0\frac{\partial\psi_1}{\partial x} + \Omega_1\frac{\partial\psi_0}{\partial x}\right\},\end{aligned} \tag{3.16}$$

$$\begin{aligned}\frac{\partial p_2}{\partial y} = {} & -\gamma\frac{\partial}{\partial y}\left\{\frac{\partial\psi_0}{\partial x}\frac{\partial\psi_1}{\partial x} + \frac{\partial\psi_0}{\partial y}\frac{\partial\psi_1}{\partial y} - \rho_1\left[\left(\frac{\partial\psi_0}{\partial x}\right)^2 + \left(\frac{\partial\psi_0}{\partial y}\right)^2\right]\right\} \\ & + \gamma\left\{\tfrac{1}{2}\rho_1\frac{\partial}{\partial y}\left[\left(\frac{\partial\psi_0}{\partial x}\right)^2 + \left(\frac{\partial\psi_0}{\partial y}\right)^2\right] + \Omega_0\frac{\partial\psi_1}{\partial y} + \Omega_1\frac{\partial\psi_0}{\partial y}\right\}.\end{aligned} \tag{3.17}$$

Equations (3.16) and (3.17) may be partially integrated for

$$\left.\begin{aligned} p_2 &= -\tfrac{1}{384}\gamma\pi^4x^4 + \tfrac{1}{128}\gamma\pi^2x^2(13 - \cos 2\pi y) + C_1(y) \\ p_2 &= -\tfrac{1}{64}\gamma\pi^2x^2\cos^2\pi y - \tfrac{1}{16}\gamma\left(\cos\pi y + \cos^2\pi y\right) + C_2(x)\end{aligned}\right\}. \tag{3.18}$$

After examining the two solutions and applying trigonometry, it is possible to combine the relations in (3.18) and deduce the second-order pressure:

$$p_2 = -\tfrac{1}{384}\gamma\pi^4x^4 + \tfrac{1}{64}\gamma\pi^2x^2(7-\cos^2\pi y) - \tfrac{1}{16}\gamma\left(\cos\pi y + \cos^2\pi y\right). \tag{3.19}$$

Determining the second-order density is a matter of substituting the pressure terms from (3.5) and (3.19) into (2.14*d*):

$$\begin{aligned}\rho_2 = {} & \tfrac{1}{384}\pi^4x^4(2-3\gamma) + \tfrac{1}{64}\pi^2x^2\left[9-2\gamma+2(\gamma-1)\cos\pi y - \cos^2\pi y\right] \\ & + \tfrac{1}{32}\left[1-\gamma+2(\gamma-2)\cos\pi y - (\gamma+1)\cos^2\pi y\right].\end{aligned} \tag{3.20}$$

Similarly, the second-order temperature becomes

$$T_2 = \tfrac{1}{192}(1-\gamma)\left[2\pi^4x^4 - 3\pi^2x^2(5+2\cos\pi y - \cos^2\pi y) + 6(1+3\cos^2\pi y)\right]. \tag{3.21}$$

4. Results and discussion

4.1. *Critical length*

To facilitate comparisons to past results, both analytical and experimental, it is convenient to normalize the axial distance by the critical length of the chamber. The latter is defined as the distance, measured from the head end, to where the flow reaches a sonic condition. For ease of calculation, the maximum axial velocity will be used to calculate the critical length. Obtaining the axial velocity and temperature at the centre-axis yields:

$$u_c = u(x,0) = \tfrac{1}{2}\pi x - \tfrac{1}{48}M_w^2\pi x\left(9-\pi^2x^2\right), \tag{4.1}$$

$$T_c = T(x,0) = 1 + \tfrac{1}{8}(\gamma-1)M_w^2\pi^2x^2 - M_w^4\tfrac{1}{96}(\gamma-1)\left(12-9\pi^2x^2+\pi^4x^4\right). \tag{4.2}$$

These expressions are obtained from substituting the results from §3 into (2.9), and evaluating the resulting expression along the centre-axis. Mathematically, the critical length is represented by the expression $\bar{u}_c/\sqrt{\gamma R\bar{T}_c} = 1$, or in terms of our dimensionless variables, $M_w u_c = \sqrt{T_c}$. Substitution of (4.1) and (4.2) into the latter produces

$$\begin{aligned}&\tfrac{1}{2304}M_w^6\pi^6x^6 + \tfrac{1}{384}M_w^4\pi^4\left[4(\gamma+1) - 3M_w^2\right]x^4 \\ &+\tfrac{1}{256}M_w^2\pi^2\left[32(\gamma+1) - 24(\gamma+1)M_w^2 + 9M_w^4\right]x^2 + \tfrac{1}{8}M_w^4(\gamma-1) - 1 = 0,\end{aligned} \tag{4.3}$$

which has the real, positive root

$$x_s = \frac{1}{\pi M_w}\sqrt{\frac{9M_w^4 + 6M_w^2\left[\phi^{1/3} - 4(\gamma+1)\right] + 8(\gamma+1)\left[4(2\gamma-1) - \phi^{1/3}\right] + \phi^{2/3}}{\phi^{1/3}}}, \tag{4.4}$$

where

$$\left.\begin{aligned}\phi &= -\beta + \sqrt{\beta^2-\alpha^3}, \\ \alpha &= 9M_w^4 - 24M_w^2(\gamma+1) + 32(2\gamma-1)(\gamma+1), \\ \beta &= 27M_w^6 + 36M_w^4(\gamma-7) - 288M_w^2(\gamma-2)(\gamma+1) \\ &\quad -128\{14+\gamma[6-\gamma(3+4\gamma)]\}.\end{aligned}\right\} \tag{4.5}$$

Equation (4.4) is only weakly dependent on the Mach number under the radical. We can find a more manageable expression for the sonic length by writing

$$x_{sa} = \frac{1}{\pi M_w}\sqrt{\frac{\phi_a^{2/3} - 8\phi_a^{1/3}(\gamma+1) + 32(2\gamma^2+\gamma-1)}{\phi_a^{1/3}}}, \tag{4.6}$$

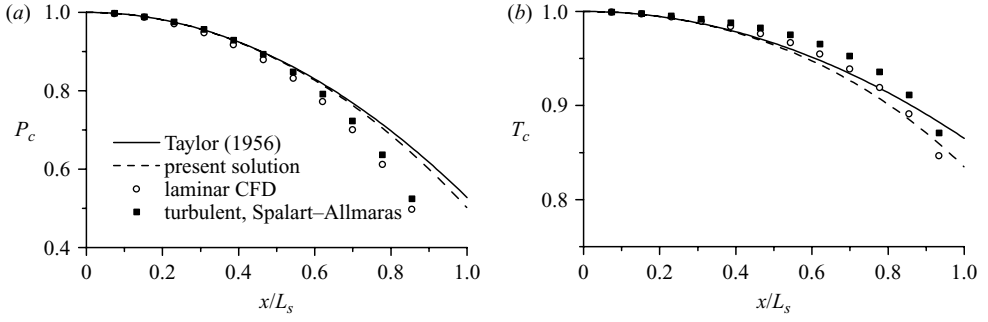

FIGURE 2. Comparison of the centre-axis (*a*) pressures and (*b*) temperatures from analytical and computational models. $\gamma = 1.4$.

where

$$\phi_a = -128[(4\gamma^3 + 3\gamma^2 - 6\gamma - 14)] + 3\sqrt{-(3\gamma^4 + 14\gamma^3 + 6\gamma^2 - 18\gamma - 22)}. \quad (4.7)$$

Equation (4.6) is accurate to the third decimal place when compared to the similar full expression of the sonic length for injection Mach numbers appropriate for rocket applications, specifically those not exceeding 0.05.

4.2. *Computational verification*

In order to ensure that the perturbation expansion is valid, a numerical verification is undertaken. A finite-volume program provides the segregated two-dimensional double-precision steady compressible solver that serves as a basis for the numerical comparison. Laminar and Spalart–Allmaras models are both used to account for the viscosity effects in the calculations. A rectangular geometry with a half-height of 1 cm, a length of 45 cm, and a grid resolution of 100×280 is used to model the slab geometry. The results are shown to be mesh independent by retaining their consistency for a number of higher-resolution grids. These dimensions match those adopted by Traineau *et al.* (1986) in their experimental and numerical investigations of the same problem. A uniform mass injection is imposed on the sidewalls of 13 kg m^{-2} s^{-1}, providing a close approximation for the constant injection velocity used in the perturbation analysis. The injectant is air with a temperature of 260 K, molecular weight of 29 kg $kmol^{-1}$, dynamic viscosity of 1.66×10^{-5} kg m^{-1} s^{-1}, and a ratio of specific heats of 1.4.

The first verification concerns the thermodynamic properties along the centre-axis of the chamber, specifically, the pressure and temperature. These terms are chosen for their ease of calculation, both numerically and analytically, as well as for their ability to provide comparisons along the entire length of the chamber.

Figure 2(*a*) compares the centre-axis pressure profile using $\gamma = 1.4$. The length scale, x/L_s, is introduced to normalize the length of the chamber by the sonic length calculated in the previous section. This normalization facilitates the comparison of chambers of varying sizes. By examining the solution presented here, good agreement is observed near the headwall, with deviations from the numerical simulation appearing as the flow progresses to the aft end. The present solution more closely matches the Spalart–Allmaras model rather than the laminar flow model. This can be attributed to the quasi-viscous nature of the solution, being driven by the normal injection condition at the walls.

The temperature comparison in figure 2(*b*) presents a slightly different contrast. As in the pressure comparison, the agreement near the headwall of the chamber is

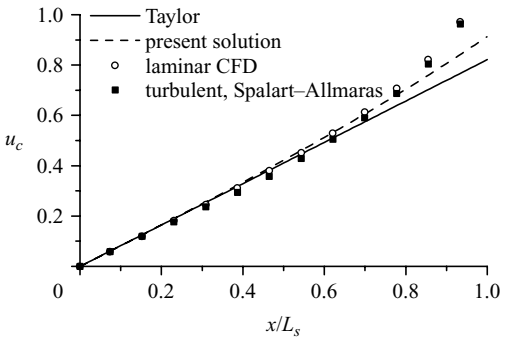

FIGURE 3. Comparison of predicted centre-axis velocity with numerical results. $\gamma = 1.4$.

excellent with deviations occurring as the flow progresses past the halfway point of the chamber. The solution approaches the numerical results as the flow nears the exit. The present analysis more closely follows the laminar numerical model, rather than the more elaborate turbulent model. This is not unexpected and can be attributed to two causes. The first is that while the normal injection condition at the walls ensures quasi-viscous behaviour, it does not account for any thermal effects that a viscous flow would introduce. Thus, the present analytical model would be expected to under-predict the centre-axis temperature. The second cause is that the energy model used to determine the temperature, namely isentropic flow, is restrictive. Relaxing the isentropicity would possibly lead to a more accurate prediction of the centre-axis temperature.

It is also of interest to compare the predicted velocity at various points in the motor chamber. Since high velocities can lead to changes in motor performance, it is important that these variations are correctly accounted for. In order to obtain meaningful comparisons throughout the motor, the centre-axis velocities are considered.

The centre-axis comparison in figure 3 shows some interesting features and generally good agreement with the numerical results. The solution resembles the numerical data early in the chamber, but then diverges under the numerical predictions near the end of the chamber. This difference can be attributed to the lack of viscous effects in our formulation. While it is true with the normal injection condition that some aspects of the solution may more closely approximate a viscous model, the effect of the normal injection decreases as the area of interest moves toward the centre-axis. The result is a parallel flow with a slightly different shape from the one accounting for viscosity. If the viscous losses were accounted for, no doubt the centre-axis velocity would have trended toward closer agreement with the numerical results.

4.3. *Theoretical and experimental comparisons*

Flow in a rectangular channel has been a topic studied in a number of different applications and, as such, has given rise to a wealth of theoretical and experimental data available to make comparisons against. Even in the relatively narrow application of the slab rocket motor, studies by Traineau *et al.* (1986) and Gany & Aharon (1999) provide both theoretical and experimental results. Taylor's incompressible solution for the slab is another useful benchmark.

The baseline for comparison is the pressure distribution at the centre-axis of the chamber (figure 4). Gany & Aharon (1999) provide a one-dimensional model for the

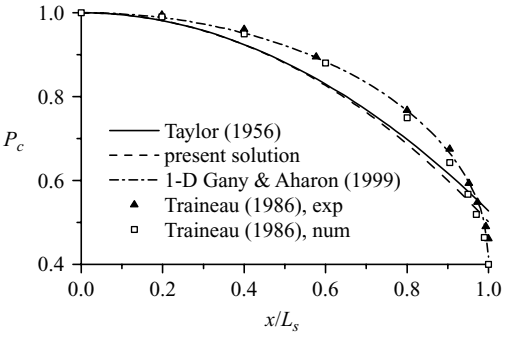

FIGURE 4. Comparison of centre-axis pressures to former studies. $\gamma = 1.4$.

pressure distribution, namely,

$$\frac{p}{p_0} = \frac{1 + \gamma[1 - (x/L)^2]^{1/2}}{1 + \gamma}. \tag{4.8}$$

Traineau supplies a pseudo-two-dimensional analysis using stream tube analysis, and experimental data to compare against. The results here are somewhat surprising. The one-dimensional model appears to closely match the experimental data for the centre-axis pressure. Traineau notes the same, along with the justification for the two-dimensional numerical simulation to under-predict the experimental data. It is possible that the introduction of viscous effects would lower the axial gradient, thus explaining the two-dimensional results from Traineau being lower than the observed experimental data. However, it does not completely explain why the one-dimensional model matches the centre-axis pressure prediction so well, while being less accurate for other variables of interest. It is speculated that the effects of viscosity cancel in the one-dimensional model since the flow is effectively injected along the centre-axis. We would then expect the relaxing of the inviscid condition to produce a shift down in the centre-axis pressure, bringing the predicted values in line with experimental results.

To assess compressibility effects on velocity profiles at varying locations in the chamber, our solution will be paired with data from Traineau's experimental and computational study. This enables us not only to observe the evolution predicted by the present model, but also to establish a comparison grounded in reality with the experimental results. Traineau collects measurements at various locations which, when normalized by the length of the motor, occur at approximately 20% increments of the total length, beginning at 40%.

The agreement of the asymptotic formulation with the experimental data shown in figure 5 is encouraging. Until the flow reaches 40% of the sonic length, the fluid is nearly incompressible, following the sinusoidal profile predicted by Taylor. However, as the flow travels further downstream, the velocity profile steepens. This steepening is found in both the experimental data and the computational verification of Traineau. It has been posited previously by Balakrishnan *et al.* (1992) that the steepening effects could be attributed to both compressibility and turbulent effects. Using the present model as a guide, we can see that at least a portion of the steepening effect can be attributed to the effects of compressibility. While the agreement between the present model and the experimental data is not perfect, we would expect that properly accounting for viscosity and possible turbulent effects would further steepen

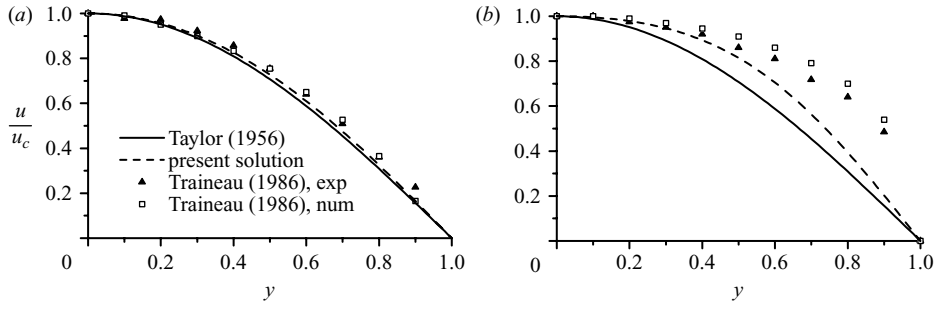

FIGURE 5. Comparison of the axial velocities at various locations. (*a*) $x/L_s = 0.4$, (*b*) 1.0.

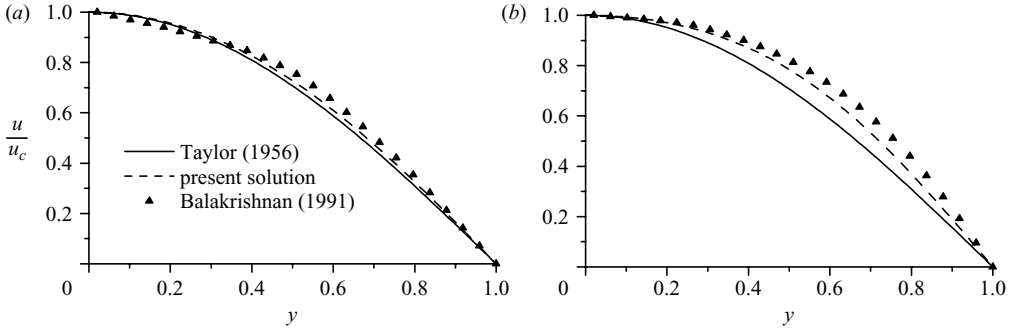

FIGURE 6. Axial velocity comparison with Balakrishnan *et al.* (1991). (*a*) $x/L_s = 0.4$, (*b*) 0.8.

the velocity profile, thus bringing it closer to agreement with the experimental measurements.

Since the work of Balakrishnan *et al.* (1991) is still the most widely cited compressible study of rocket motors, a comparison to the present investigation is made in figure 6. Figure 6(*a*) depicts the velocity profile at $x/L_s = 0.4$, before the effects of compressibility become dominant. Here, the velocity profiles of the incompressible baseline, the present work, and the Balakrishnan numerical study are all in close agreement. In figure 6(*b*), the flow is near the critical point at $x/L_s = 0.8$, so compressibility effects are more pronounced. The present analysis shows good agreement with the results of Balakrishnan's study. While the present solution slightly underpredicts the Balakrishnan work, it has the benefit of providing a simple closed-form analytical alternative; Balakrishnan's results are obtained by numerically integrating a reduced equation that is arrived at using two assumptions not considered here: a sufficiently long, slender chamber, and purely axial dependence in the radial momentum equation.

4.4. *Streamlines*

The behaviour of the streamlines is illustrated by figure 7. The solid lines depict the incompressible streamlines and the dotted lines display the effects of compressibility. When compressibility effects are accounted for, the streamlines turn more rapidly, thus generating a steeper profile. As the injection velocity is increased, the behaviour becomes more pronounced, and deviations from the incompressible condition are observed earlier in the flow. As the injection Mach number is increased, the distance required for the flow to reach sonic conditions quickly decreases. This behaviour is

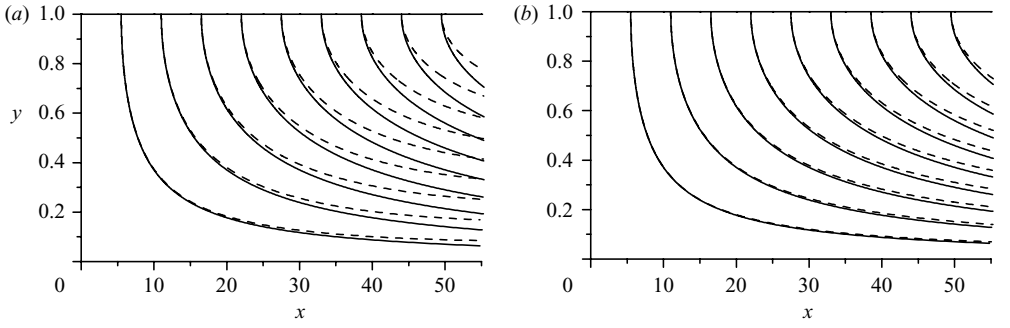

FIGURE 7. An illustration of the effects of compressibility on the streamlines. The solid lines represent the incompressible solution and the dashed lines depict the compressible solution. (*a*) $M_w = 0.01$, (*b*) 0.006.

reflective of a strong correlation between the critical distance and M_w, as alluded to in §4.1.

Near the headwall, the effects of compressibility are negligible, a behaviour that was previously observed in the numerical simulation. As the fluid travels toward the aft end and increases in speed, compressibility effects become more pronounced. Using the streamline plot as a guide, it is possible to calculate the point where the magnification of the velocity via compressibility becomes so large that it must be accounted for.

4.5. *Compressible design criterion*

We can define a set of criteria for measuring the effects of compressibility. The first criterion is the compressibility ratio,

$$\chi_c = \frac{u(x,0)}{u_0(x,0)}. \tag{4.9}$$

This is simply the ratio between the compressible and incompressible velocities. It represents the amplification of the centre-axis velocity at a given location in the chamber.

It is possible to obtain an analytical expression for the compressible amplification via substitution of (2.9) and (2.10) into (4.9). These yield

$$\chi_c = 1 + \tfrac{1}{24} M_w^2 \left(\pi^2 x^2 - 9\right). \tag{4.10}$$

One way to make use of the formulation in (4.10) effectively is to introduce an acceptable error, here labelled ϵ. If we know that a velocity error of up to 5% is acceptable, we let $\chi_c = 1 + \epsilon$. With this substitution and subsequent simplification, (4.10) becomes

$$x_\epsilon = \sqrt{\frac{24\epsilon}{M_w^2 \pi^2} + \frac{9}{\pi^2}}. \tag{4.11}$$

Equation (4.11) represents an expression for the location in the chamber where an error of ϵ is first introduced. However, to find a reasonable approximation, the $9/\pi^2$ may be ignored as the first term in the equation dominates for typical values expected in rocket design; we are left with

$$x_\epsilon = \frac{2\sqrt{6\epsilon}}{M_w \pi}. \tag{4.12}$$

Conversely, if the geometry of the chamber is fixed, we can obtain a rough approximation of the maximum injection Mach number by rearranging the equation to yield $2\sqrt{6\epsilon}/(\pi x)$. Since calculations of this type often degrade in the vicinity of the nozzle, it is common practice to specify that an error is acceptable if it is limited to a small fraction of the chamber length near the nozzle. We can thus introduce $x = (1 - z)L$, where z is the segment along which the error may exceed ϵ (the last 1/8 for example), and $L = L_0/a$ is the aspect ratio of the chamber. This substitution yields

$$M_w^* = \frac{2\sqrt{6\epsilon}}{\pi(1 - z)L}. \tag{4.13}$$

The validity of these criteria is easily verifiable. The compressibility criteria set forth in (4.12) and (4.13) were actually used to select the streamfunction plots shown in figure 7. This was accomplished by allowing a 5% deviation in the last eighth of the motor. In figure 7(*a*), it is advisable to absorb the extra complexity of the compressible model in favour of the more accurate flow-field prediction. From a cursory examination of the streamlines, we can see significant deviations from the incompressible flow model almost immediately. In the second, less extreme, case shown in figure 7(*b*), the effects of compressibility are relatively negligible. Steepening of the streamlines is observed, but not to an appreciable level.

4.6. *Internal ballistics*

Since the primary variables are known at any position in the chamber, it is possible to calculate secondary performance characteristics. More so than velocity profiles or streamline plots, these ballistics terms are at the heart of rocket analysis. In what follows, we determine some of the critical ballistics criteria that arise in practical analyses of nozzleless rocket motors.

4.6.1. *Specific impulse*

First an expression for the total mass flow rate at any given cross-section may be determined to good approximation by

$$\begin{aligned} \dot{m} &= \int \rho u \, \mathrm{d}A = 2w \int_0^1 \rho u \, \mathrm{d}y \\ &= \tfrac{1}{2304} U_w \rho_0 h^2 w x (M_w^2 \pi^2 x^2 + 12) \\ &\quad \times \left[M_w^4 \pi^4 x^4 (2 - 3\gamma) - 48 M_w^2 \pi^2 x^2 + 384 \right] + O(M_w^5), \end{aligned} \tag{4.14}$$

where $w = \bar{w}/h$. This equation is accurate to three significant digits for the range of operation of most motors.

The thrust force for a given motor length can be expressed as

$$\begin{aligned} F &= \int \rho u^2 \, \mathrm{d}A = 2w \int_0^1 \rho u^2 \, \mathrm{d}y \\ &= \tfrac{1}{1536} h^2 \rho_0 U_w^2 \pi^2 x^2 w (\tfrac{29}{4608} M_w^4 \pi^4 x^4 + \tfrac{7}{48} M_w^2 \pi^2 x^2 + 1) \\ &\quad \times \left[M_w^4 \pi^4 x^4 (2 - 3\gamma) - 48 M_w^2 \pi^2 x^2 + 384 \right] + O(M_w^5). \end{aligned} \tag{4.15}$$

Equation (4.15) is also an approximate expression for the thrust force, accurate to three significant digits.

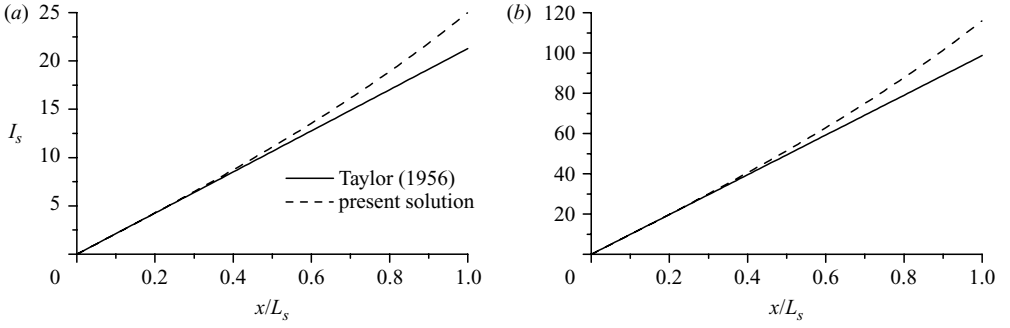

FIGURE 8. The specific impulse for (*a*) $a_0 = 323$ m s^{-1} and (*b*) $a_0 = 1500$ m s^{-1}.

When the thrust force is divided by the mass flux and the standard acceleration of gravity at sea level, we can determine the specific impulse, namely,

$$I_s = \frac{F}{\dot{m} g_0} = \frac{U_w}{3072 g_0} \pi^2 x (M_w^2 \pi^2 x^2 + 12)^{-1} \times (29 M_w^4 \pi^4 x^4 + 672 M_w^2 \pi^2 x^2 + 4608) + O(M_w^5). \tag{4.16}$$

Note that I_s is independent of the motor cross-section.

If compressibility effects are ignored, the specific impulse becomes

$$(I_s)_{inc} = \frac{\pi^2 U_w}{8 g_0} x. \tag{4.17}$$

A comparison of the two terms over the length of a typical motor is presented in figure 8. The first case corresponds to the cold-flow injection of air used by Traineau *et al.* (1986). A second hot-flow case is shown for a motor of similar size to cover a more realistic range of values for the specific impulse. Near the headwall, both the compressible and incompressible specific impulses follow the same linear relationship. Once the flow nears the midpoint of the chamber, the compressible expression diverges as the nonlinear terms in (4.16) begin to dominate. Note that the axial distributions in figures 8(*a*) and 8(*b*) have similar relative proportions. This is easily explained by the common dependence on the injection velocity, U_w. In (4.16) and (4.17), U_w appears as a scaling parameter, multiplying both expressions equally.

It is also of interest to note that by scaling the length of the chamber by the critical distance, the specific impulse curve for a given value of U_w will be the same for a variety of chambers. For example, figure 8 is generated using values based on Traineau's experimental case with $L_s = 45.5$. If we select a lower value for injection, say $M_w = 0.0034$ and $L_s = 153.78$, creation of a similar plot will produce curves that are identical to figure 8, despite their smaller injection Mach number.

4.6.2. *Characteristic velocity*

Another value of merit is the characteristic velocity, c^*. The characteristic velocity is a comparative measure of propellant and combustion system performance. Because c^* is independent of the nozzle performance, it is ideal for evaluating nozzleless rocket performance. Sutton & Biblarz (2001) define c^* as

$$c^* = \frac{p_c A_t}{\dot{m}}. \tag{4.18}$$

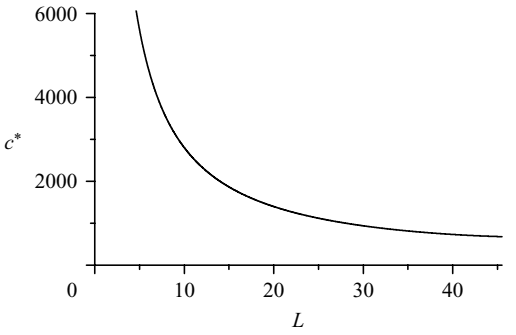

FIGURE 9. Evolution of the characteristic velocity for $M_w = 0.0115$ and $a_0 = 323$ m s^{-1}. $\gamma = 1.4$.

where p_c is the combustion chamber pressure, A_t is the throat area of the nozzle, and $\dot{m}$ is the mass flow rate through the motor. Because our analysis is not limited by a constant pressure throughout the combustion chamber, an average value of the chamber pressure may be readily calculated from

$$p_c = \frac{\int p \, \mathrm{d}V}{V} = \frac{p_0}{L} \int_0^1 \int_0^L p \, \mathrm{d}x \, \mathrm{d}y$$
$$= p_0 \left[1 - M_w^2 \gamma \left(\tfrac{1}{4} + \tfrac{1}{24}\pi^2 L^2 + \tfrac{1}{32} M_w^2 - \tfrac{13}{384}\pi^2 L^2 M_w^2 + \tfrac{1}{1920}\pi^4 L^4 M_w^2\right)\right]. \quad (4.19)$$

At the outset, we find

$$c^* = \frac{12 a_0^2 \left[-1920/\gamma + 80 M_w^2 \left(6 + L^2\pi^2\right) + M_w^4 \left(60 - 65 L^2\pi^2 + L^4\pi^4\right)\right]}{5 L U_w \left(12 + L^2 M_w^2 \pi^2\right) \left[-384 + 48 L^2 M_w^2 \pi^2 + L^4 M_w^4 \pi^4 (3\gamma - 2)\right]}. \quad (4.20)$$

Figure 9 depicts the characteristic velocity for motors of varying length. Unsurprisingly, the expression in (4.20) is singular at the origin, being strongly dependent on the length of the motor. For short chambers, $c^* \to \infty$. When the length of the motor increases to the practical range of aspect ratios, the values of the characteristic velocity quickly fall in line with the normal range of values expected for solid rocket motor operation. The shape of the plot in figure 9 suggests that while smaller chambers may be more efficient, efficiency is nearly invariant in longer motors since the curve approaches a fixed value as the length of the motor is extended.

5. Conclusion

The Rayleigh–Janzen perturbation approach presented here produces a compact closed-form solution with results that are in good agreement with both computation and experiment. The closed-form expressions for the variables of interest help to further the understanding of compressibility effects on the flow field of a surface-injection-driven chamber, where previously only numerical or experimental predictions were tenable. Variations from the numerical analysis in pressure can be accounted for by the neglect of viscosity. The temperature is affected by the absence of viscosity and the isentropic assumption. Further analysis using a more complete energy model is suggested in an attempt to bring the temperature predictions to closer agreement with numerical values. In addition to advancement of compressible flow theory, practical relations are presented to aid the design of both regular and nozzleless rockets.

This project was sponsored by the National Science Foundation through NSF Grant CMS-0353518 and, through matching funds, by the University of Tennessee Space Institute (UTSI). The authors are deeply grateful for the support received from the NSF Program Director, Dr Eduardo A. Misawa.

Appendix. First-order streamfunction

Since $f(\psi_0)$ is used to satisfy the boundary conditions, it is expected that the $f(\psi_0)$ term will follow the form of the right-hand side. To this end, we posit

$$f(\psi_0) = A_1 x \sin\left(\tfrac{1}{2}\pi y\right) + A_2 x^3 \sin^3\left(\tfrac{1}{2}\pi y\right). \tag{A 1}$$

To further simplify bookkeeping, we let $\eta = \pi y/2$. Next, a solution is assumed of the form

$$\psi_1(x, \eta) = x g(\eta) + x^3 h(\eta). \tag{A 2}$$

Substitution into (3.14) yields

$$\begin{aligned}&\tfrac{1}{4}\pi^2\left[x\left(g'' + g\right) + x^3\left(h'' + h\right)\right] + 6xh \\ &\quad = -\tfrac{1}{4}\pi^2 x \sin(\eta)\left[-\tfrac{1}{4}\pi^2 x^2 + 1 + \cos(2\eta)\right] + A_1 x \sin\eta + A_2 x^3 \sin^3\eta,\end{aligned} \tag{A 3}$$

where the primed quantities represent derivatives with respect to η. Equation (A 3) simplifies by grouping all terms in powers of x. We obtain

$$\begin{aligned}&x^3\left[\tfrac{1}{4}\pi^2\left(h'' + h - \tfrac{1}{4}\pi^2\sin\eta\right) - A_1\sin^3\eta\right] \\ &\quad + x\left[\tfrac{1}{4}\pi^2\left(g'' + g + \sin\eta + \cos 2\eta\sin\eta\right) + 6h - A_2\sin\eta\right] = 0.\end{aligned} \tag{A 4}$$

In order for (A 4) to be true for all values of x, the bracketed quantities multiplying both the x^3 and x terms must each be set to zero. The partial differential equation may thus be written as two ordinary differential equations:

$$h'' + h = \tfrac{1}{4}\pi^2\sin\eta + A_1\sin^3\eta, \tag{A 5}$$

$$g'' + g = \frac{4}{\pi^2}\left(A_2\sin\eta - 6h\right) - \sin\eta - \cos 2\eta\sin\eta. \tag{A 6}$$

Equation (A 5) yields

$$\begin{aligned}h = C_1\cos\eta + C_2\sin\eta + \tfrac{1}{16}\pi^2\left(\cos\eta\sin 2\eta - 2\eta\cos\eta - \sin\eta - \cos 2\eta\sin\eta\right) \\ + \frac{A_1}{8\pi^2}\left(\cos 4\eta\sin\eta + 8\cos\eta\sin 2\eta - 12\eta\cos\eta - 4\cos 2\eta\sin\eta - \cos\eta\sin 4\eta\right).\end{aligned} \tag{A 7}$$

This may then be substituted at the right-hand side of (A 6) so that all of the non-homogeneous terms are determined. This follows the same methodology as used to determine (A 7). We obtain

$$\begin{aligned}g = C_3\cos\eta + C_4\sin\eta + \frac{A_1}{16\pi^4}[144\left(\eta\cos\eta + \eta\cos\eta\cos 2\eta + \eta^2\sin\eta + \eta\sin\eta\sin 2\eta\right) \\ +156\cos 2\eta\sin\eta - 132\cos\eta\sin 2\eta + 6\left(\cos 4\eta\sin\eta - \cos\eta\sin 4\eta\right)] \\ + \frac{A_2}{\pi^2}(\cos\eta\sin 2\eta - 2\eta\cos\eta - \cos 2\eta\sin\eta) - \frac{6C_1}{\pi^2}(\cos\eta\cos 2\eta + 2\eta\sin\eta + \sin\eta\sin 2\eta) \\ + \frac{6C_2}{\pi^2}(\cos 2\eta\sin\eta + 2\eta\cos\eta - \cos\eta\sin 2\eta) \\ + \tfrac{1}{16}[12\left(\eta\cos\eta\cos 2\eta + \eta^2\sin\eta + \eta\sin\eta\sin 2\eta\right) + 10\cos 2\eta\sin\eta \\ -6\cos\eta\sin 2\eta + 4\eta\cos\eta + \cos 4\eta\sin\eta - \cos\eta\sin 4\eta].\end{aligned} \tag{A 8}$$

Now the relationships for h and g may be substituted into (A 2); we obtain

$$\begin{aligned}\psi_1 = \frac{1}{16\pi^4}x(&-2\cos\eta\{12A_1\eta(\pi^2x^2-12)\\&+\pi^2[16A_2\eta+\pi^4x^2\eta+48(C_1-2\eta C_2)-8\pi^2(\eta+x^2C_1+C_3)]\}\\&+4\sin\eta\{3A_1[\pi^2x^2+12(\eta^2-1)]+\pi^2[4A_2-24(2\eta C_1+C_2)\\&+\pi^2(-2+3\eta^2+4x^2C_2+4C_4)]\}+\sin 3\eta[\pi^4+2A_1(\pi^2x^2+3)].\end{aligned} \tag{A 9}$$

While (A 9) does not appear to be a simple expression, potential for simplification stems from administering the boundary conditions. The solution for the undetermined coefficients follows the same method as pursued earlier in the determination of the leading-order coefficients. We first examine the no flow across the centre-axis from (2.15); recalling that it is evaluated at $(x, 0)$, we can put

$$-\frac{6C_1}{\pi^2}+C_3+3x^2C_1=0. \tag{A 10}$$

In order for this equation to be true $\forall x$, the coefficients multiplying the x^2 and the x^0 terms must vanish independently. This single boundary condition may actually be used as two equations that render

$$C_1=0, \quad C_3=0. \tag{A 11}$$

Revisiting (2.15), we have

$$\begin{aligned}&\frac{1}{16\pi^4}x^3\left(6A_1\pi^4+\tfrac{1}{2}\pi^8\right)\\&+\frac{1}{16\pi^4}x\left[-72A_1\pi^2+8A_2\pi^4-4\pi^6+4\left(18A_1\pi^2+\tfrac{1}{2}3\pi^6\right)-48\pi^4C_2\right]=0.\end{aligned} \tag{A 12}$$

This may be turned into two equations such that (A 12) holds for all values of x:

$$A_1=-\tfrac{1}{12}\pi^4, \quad 8A_2\pi^4+2\pi^6-48\pi^4C_2=0. \tag{A 13}$$

At this juncture, it is advantageous to apply the final boundary condition from (2.15), namely,

$$x^2\left(3C_2-\tfrac{1}{32}\pi^2\right)+C_4+\frac{21}{32}+\frac{A_2}{\pi^2}-\frac{6C_2}{\pi^2}=0. \tag{A 14}$$

This, in turn, gives

$$C_2=\tfrac{1}{96}\pi^2, \quad C_4+\frac{21}{32}+\frac{A_2}{\pi^2}=0. \tag{A 15}$$

Solving (A 13) and (A 15) simultaneously determines the final two constants

$$A_2=-\tfrac{3}{16}\pi^2, \qquad C_4=-\frac{15}{32}. \tag{A 16}$$

REFERENCES

Apte, S. & Yang, V. 2001 Unsteady flow evolution in a porous chamber with surface mass injection. Part I: Free oscillation. *AIAA J.* **39**, 1577–1586.

Balachandar, S., Buckmaster, J. D. & Short, M. 2001 The generation of axial vorticity in solid-propellant rocket-motor flows. *J. Fluid Mech.* **429**, 283–305.

Balakrishnan, G., Liñán, A. & Williams, F. A. 1991 Compressible effects in thin channels with injection. *AIAA J.* **29**, 2149–2154.

Balakrishnan, G., Liñán, A. & Williams, F. A. 1992 Rotational inviscid flow in laterally burning solid propellant rocket motors. *J. Propul. Power* **8**, 1167–1176.

Beddini, R. A. & Roberts, T. A. 1988 Turbularization of an acoustic boundary layer on a transpiring surface. *AIAA J.* **26** (8), 917–923.

Beddini, R. A. & Roberts, T. A. 1992 Response of propellant combustion to a turbulent acoustic boundary layer. *J. Propul. Power* **8**, 290–296.

Berman, A. S. 1953 Laminar flow in channels with porous walls. *J. Appl. Phys.* **24**, 1232–1235.

Casalis, G., Avalon, G. & Pineau, J.-P. 1998 Spatial instability of planar channel flow with fluid injection through porous walls. *Phys. Fluids* **10**, 2558–2568.

Chu, W.-W., Yang, V. & Majdalani, J. 2003 Premixed flame response to acoustic waves in a porous-walled chamber with surface mass injection. *Combust. Flame* **133**, 359–370.

Culick, F. E. C. 1966 Rotational axisymmetric mean flow and damping of acoustic waves in a solid propellant rocket. *AIAA J.* **4**, 1462–1464.

Flandro, G. A. 1980 Stability prediction for solid propellant rocket motors with high-speed mean flow. Final Tech. AFRPL-TR-79-98. Air Force Rocket Propulsion Laboratory, Edwards AFB, CA.

Gany, A. & Aharon, I. 1999 Internal ballistics considerations of nozzleless rocket motors. *J. Propul. Power* **15**, 866–873.

Janzen, O. 1913 Beitrag zu Einer Theorie der Stationaren Stromung Kompressibler Flussigkeiten. *Phys. Z.* **14**, 639–643.

Kaplan, C. 1943 The flow of a compressible fluid past a curved surface. *NACA TR* 768.

Kaplan, C. 1944 The flow of a compressible fluid past a circular arc profile. *NACA TR* 994.

Kaplan, C. 1946 Effect of compressibility at high subsonic velocities on the lifting force acting on an elliptic cylinder. *NACA TR* 834.

King, M. K. 1987 Consideration of two-dimensional flow effects on nozzleless rocket performance. *J. Propul. Power* **3**, 194–195.

Maicke, B. A. & Majdalani, J. 2006 The compressible Taylor flow in slab rocket motors. In *AIAA Paper* 2006-4957.

Majdalani, J. 2001 The oscillatory channel flow with arbitrary wall injection. *Z. Angew Math. Phys.* **52**, 33–61.

Majdalani, J. 2005 The compressible Taylor–Culick flow. In *AIAA Paper* 2005-3542.

Majdalani, J. 2007 On steady rotational high speed flows: The compressible Taylor–Culick profile. *Proc. R. Soc. Lond.* A **463**, 131–162.

Majdalani, J., Vyas, A. B. & Flandro, G. A. 2002 Higher mean-flow approximation for a solid rocket motor with radially regressing walls. *AIAA J.* **40**, 1780–1788.

Meiron, D. I., Moore, D. W. & Pullin, D. I. 2000 On steady compressible flows with compact vorticity; the compressible Stuart vortex. *J. Fluid Mech.* **409**, 29–49.

Moore, D. W. & Pullin, D. I. 1998 On steady compressible flows with compact vorticity; the compressible Hill's spherical vortex. *J. Fluid Mech.* **374**, 285–303.

Najjar, F. M., Haselbacher, A., Ferry, J. P., Wasistho, B., Balachandar, S. & Moser, R. 2003 Large-scale multiphase large-eddy simulation of flows in solid-rocket motors. In *AIAA Paper* 2003-3700.

Peng, Y. & Yuan, S. W. 1965 Laminar pipe flow with mass transfer cooling. *Trans. ASME* C: *J. Heat Transfer* **87**, 252–258.

Proudman, I. 1960 An example of steady laminar flow at large Reynolds number. *J. Fluid Mech.* **9**, 593–612.

Rayleigh, Lord 1916 On the flow of a compressible fluid past an obstacle. *Phil. Mag.* **32**, 1–6.

Shapiro, A. H. 1953 *The Dynamics and Thermodynamics of Compressible Fluid Flow*, vol. 1. Ronald.

Staab, P. L. & Kassoy, D. R. 1996 Three-dimensional, unsteady, acoustic-shear flow dynamics in a cylinder with sidewall mass addition. *Phys. Fluids* **9**, 3753–3763.

Sutton, G. P. & Biblarz, O. 2001 *Rocket Propulsion Elements*, 7th edn. John Wiley.

Taylor, G. I. 1956 Fluid flow in regions bounded by porous surfaces. *Proc. R. Soc. Lond.* A **234**, 456–475.

Traineau, J.-C., Hervat, P. & Kuentamann, P. 1986 Cold-flow simulation of a two-dimensional nozzleless solid rocket motor. In *AIAA Paper* 86-1447.

Vuillot, F. & Avalon, G. 1991 Acoustic boundary layers in solid propellant rocket motors using Navier–Stokes equations. *J. Propul. Power* **7**, 231–239.

Wasistho, B., Balachandar, R. & Moser, R. D. 2004 Compressible wall-injection flows in laminar, transitional, and turbulent regimes: Numerical prediction. *J. Space Rockets* **41**, 915–924.

Yuan, S. W. 1956 Further investigation of laminar flow in channels with porous walls. *J. Appl. Phys.* **27**, 267–269.

Yuan, S. W. 1959 Cooling by protective fluid films. In *Turbulent Flows and Heat Transfer* (ed. C. C. Lin), vol. 5. Princeton University Press.

Zhou, C. & Majdalani, J. 2002 Improved mean flow solution for slab rocket motors with regressing walls. *J. Propul. Power* **18**, 703–711.